



Augmentation of absorption channels induced by wave-chaos effects in free-standing nanowire arrays

Ji-HWAN KIM,^{1,5}  SUNG BUM KANG,^{2,5} HYEON-HYE YU,^{1,5}
JAEWON KIM,³ JINHYEOK RYU,¹ JI-WON LEE,⁴ KYOUNG JIN
CHOI,^{2,6} CHIL-MIN KIM,^{1,7} AND CHANG-HWAN YI^{1,8}

¹Department of Emerging Materials Science, DGIST, Daegu 42988, South Korea

²Department of Materials Science and Engineering, UNIST, Ulsan 44919, South Korea

³Institut für Physik, Technische Universität Ilmenau, D-98693 Ilmenau, Germany

⁴Samsung Electro-Mechanics, Suwon 16674, South Korea

⁵These authors contributed equally to this work

⁶choi@unist.ac.kr

⁷chmkim@dgist.ac.kr

⁸innissan@dgist.ac.kr

Abstract: Plenty of issues on quantal features in chaotic systems have been raised since chaos was accepted as one of the intrinsic properties of nature. Through intensive studies, it was revealed that resonance spectra in chaotic systems exhibit complicated structures, which is deeply concerned with sophisticated resonance dynamics. Motivated by these phenomena, we investigate light absorption characteristics of chaotic nanowires in an array. According to our results, a chaotic cross-section of a nanowire induces a remarkable augmentation of absorption channels, that is, an increasing number of absorption modes leads to substantial light absorption enhancement, as the deformation of cross-section increases. We experimentally demonstrate the light absorption enhancement with free-standing Si-nanowire polydimethylsiloxane (PDMS) composites. Our results are applicable not only to transparent solar cells but also to complementary metal-oxide-semiconductor (CMOS) image sensors to maximize absorption efficiency.

© 2020 Optical Society of America under the terms of the [OSA Open Access Publishing Agreement](#)

1. Introduction

A nanowire is a quasi-three-dimensional nanostructure in which a quantum (wave) mechanical interpretation is more relevant than a classical one. Based on this nanowire framework, a wide range of devices, such as lasers [1], sensors [2], and photovoltaics [3], have been developed. For semiconductor-nanowire-photovoltaics, e.g., in solar cells [4] and CMOS image sensors [5], because the improvement of light absorption efficiency is crucial in maximizing yield in real applications, extensive efforts have been made to find an ideal structure of a nanowire array. Once, in a cylindrical nanowire, parameters such as radius, height, and pitch were controlled to optimize reflection, transmission, and mode excitation [6–8]. Afterward, a more path-breaking approach was proposed, such as the dielectric core-shell structure, which can achieve a balance between the absorption enhancement induced by leaky mode resonances (LMRs) and the anti-reflection effect of dielectric materials [9–12]. In addition, trials in a different direction were performed to manipulate configurations of a wire array, such as square, triangular, Penrose, and random fashion structures [13,14]. As a totally different approach, there have been studies addressing deformation of wire morphologies, such as dual-diameter, nanocone, diameter-modulated, and slanted nanowires [15–18]. Also, there were important related studies that engineer the optical properties of grating-structured nanowires made of various materials [19–21].

Recently, it was shown that the average decay rate of modes converges to a specific value improving the energy storage capacity, that is, light absorption, in chaotic resonators whose cross-sectional shape is a stadium [22]. After this remarkable finding, it was shown that the chaotic ray dynamics could be utilized to realize nanostructured black bodies, i.e., perfect absorber, that can far-advance the applicability of disordered nanostructures [23]. In addition to those advantages of chaotic systems in the light absorption and storage capability, here, we demonstrate another excellent chaotic effect on the light absorption mechanism in nanowires: augmentation of absorption channels in chaotic free-standing nanowire arrays. The main cause of chaos in our system stems from the cross-sectional shape of wires, which can be assumed to be the two-dimensional system. For several decades, two-dimensional chaotic systems deformed from a circle have been extensively studied in the quantum chaos community, and various interesting topics have been discussed across the classical, semiclassical, and quantum (wave) physical regimes. One essential property of chaotic (or non-integrable) systems is that there are a bunch of complicated mode couplings resulting in the Wigner distributions in the nearest-neighbour-spacing statistics of modes: breaking degeneracies of modes. Because this property is a dual face of classical chaos reflected in wave dynamics due to mode interactions, it is referred to as the "wave chaos" effect [24].

It is known that there are two types of mode coupling phenomena in a two-dimensional chaotic cavity: mode splittings due to the breaking of degeneracy [25] and avoided crossings [26]. As a consequence of these mode couplings, resonance spectra in the chaotic cavity exhibit greatly complicated structures [24], which provides augmented absorption channels for the strong light absorption enhancement. To demonstrate our claims explicitly, we perform optical three-dimensional simulations for a stadium-shaped cross-section nanowire in an array with the finite-difference time-domain (FDTD) method. By comparing the number of excited resonance modes in the absorption spectrum and the total absorption rate at each deformation parameter, we analyze the proportionality between them. Through this analysis, we elucidate the fact that a larger number of modes can get engaged in light absorption spectra of nanowires by means of mode splittings and avoided crossings when the cross-sectional shape is deformed from a circle to a stadium. Our discovery is experimentally verified in a silicon nanowire array having a stadium-shaped cross-section, in which broadband absorption is higher by 16.83% compared to that of a cylindrical nanowire. Moreover, it is revealed that the wavelength-resolved absorption enhancement reaches almost 4-fold in our work.

2. Chaotic cross-sectional nanowires

The stadium shape is a representative of a fully chaotic two-dimensional system, which comprises of two half-circles of radius R and two linear sections of length $2L$, as shown in Fig. 1(a). When a deformation parameter defined as $\varepsilon \equiv L/R$ is $\varepsilon \neq 0$, the classical ray dynamics in phase space are ergodic [27]. To show the effect of the chaotic cross-section of nanowires in an array, we set a rectangular nanowire array structure with a height h and a pitch a , as shown in Fig. 1(b). In nanowire arrays, the leaky waveguide modes in individual nanowires dominantly govern the light absorption rate when the photonic lattice constant is large enough [28,29]. Furthermore, when the waveguide height is much larger than examined wavelengths the electric fields in waveguides can be expressed by the factorization form [30], as follows: $E(x, y, z) = e(x, y)\exp(i\beta z)$. In other words, the chaotic properties of a cross-section of the nanowire directly affect the electromagnetic fields of the nanowire by perturbing $e(x, y)$. Under this condition, an ε -dependent absorption spectrum is obtained by using the FDTD method. Over the entire calculation procedure, we preserve the cross-sectional area of wires to compare the light absorption rate for the same volume at the fixed height of wires. Because of this area preservation, the length of the linear section $L(\varepsilon) = \varepsilon\sqrt{A}/\sqrt{\pi + 4\varepsilon}$ increases, while the radius $R(\varepsilon) = \sqrt{A}/\sqrt{\pi + 4\varepsilon}$ decreases, as ε increases when the cross-sectional area of a cylindrical nanowire is $A = \pi R_0^2$ at $\varepsilon = 0.0$.

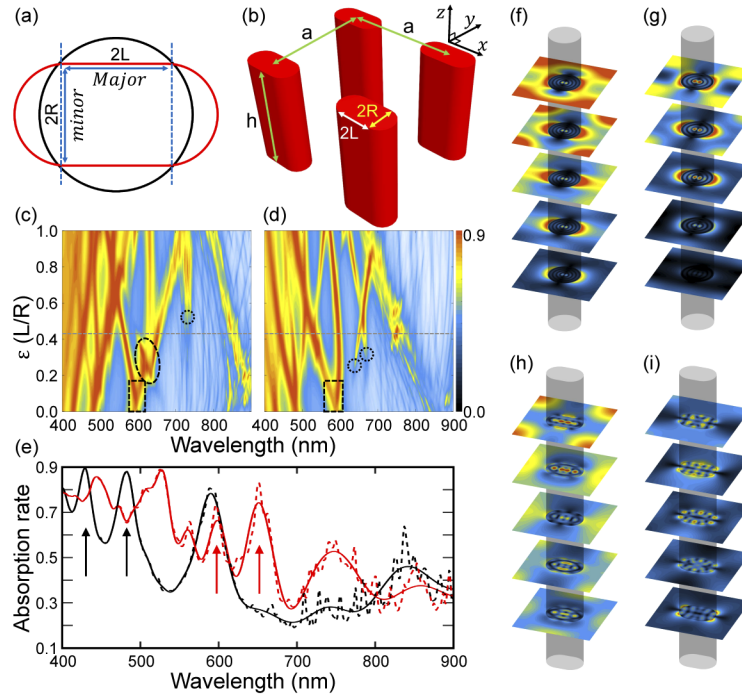


Fig. 1. Morphology of a chaotic-nanowire array and absorption spectra. (a) The cross-section of a circle (black-solid curve) and a stadium shape (red-solid curve), where $2L$ and R are a length of linear section and a radius of half circle, respectively. (b) The schematic illustration of a nanowire array structure consisting of a pitch a and a height h . (c) and (d) The absorption spectra as functions of $\varepsilon \equiv L/R$ and λ , when an incident light is illuminated along the negative- z direction with a polarization along the major and the minor axis, respectively. The color-code stands for the dimensionless absorption rate. Representative examples of the bifurcations, emergences, and avoided crossings of absorption peaks are marked by the dashed boxes, the dotted circles, and the dashed ellipse, respectively. (e) The absorption spectrum of the Si nanowire array at $\varepsilon=0.0$ (black-dotted curve) and 0.43 (red-dotted curve) for unpolarized light, i.e., the sum of (c) and (d). The overlaid solid curves are the same spectra, but the FP modes are excluded (see text). (f) and (g) are spatial distributions of absorption intensities in a circular ($\varepsilon = 0$) nanowire array for the wavelengths indicated by the black arrows in (e) at arbitrarily selected heights. (h) and (i) are the spatial distribution of absorption intensities in a stadium ($\varepsilon = 0.43$) nanowire array for the wavelengths indicated by the red arrows in (e). The red color represents the high intensity and the black, the low one, in arbitrary unit.

3. Numerical simulation

3.1. Simulation setup of Si nanowire arrays

The light absorption rate of nanowire arrays is numerically simulated by the Lumerical finite-difference time-domain (FDTD), which is the commercial software solving time-dependent Maxwell's equations. In the simulations, we used the refractive index of Si offered in the built-in database of the Lumerical FDTD. The individual nanowires in arrays have radii $R = 100$ nm and 200 nm and are surrounded by an air background having the refractive index $n=1$. For excitation of nanowires, a plane-wave incident light, whose propagation direction is parallel to the nanowire, is used for all calculations in this work. The periodic boundary condition was used in x and y directions, and the perfect matched layer boundary was used in z direction. For the absorption

and reflection spectra and for time-resolved reflected light of the nanowire, the simulations were performed using the same parameters as those employed in the experiments.

3.2. Light absorption spectra

At the first stage, we compute the absorption spectrum for $R_0 = 200$ nm, $h = 4$ μ m, and $a = 1$ μ m as a function of ε , $0.0 \leq \varepsilon \leq 1.0$, in the wavelength range, $400 \leq \lambda \leq 900$ nm. Because the stadium shape has mirror reflection symmetries with respect to both the major and minor axes [see, Fig. 1(a)], two linearly polarized light along these axes are considered. Figures 1(c) and (d) show the absorption spectrum when the polarization of the incident light is along the major and the minor axis, respectively. In these two figures, one can see, roughly, three main absorption peaks at $\varepsilon = 0.0$ for $\lambda < 700$ nm. Because a circle is isotropic, the two spectra of different polarization at $\varepsilon = 0.0$ are the same. However, in a higher ε region, the complicated absorption spectra of the two figures are very different. This difference can be understood in terms of bifurcations (in dashed boxes), emerging of absorption peaks (in dotted circles), and avoided resonance crossings (in dashed ellipses), which depends both on the deformation and polarization.

To show the wave-chaos property engaging in absorption rate more clearly, we compare the absorption spectra at $\varepsilon=0$ and 0.43. Because light in nature is unpolarized, we obtain the total absorption rate by averaging the absorption rate of the two differently polarized incident lights. The black-dashed and the red-dashed curve in Fig. 1(e) are those for $\varepsilon=0$ and 0.43, respectively. The separated absorption spectrum for each of the two polarized incident lights is given in Fig. 5 in Appendix. The short period fluctuations, which can be observed more clearly in $\lambda > 700$ nm, are consequences of the Fabry-Perot (FP)-type modes along the wire-axis. This FP-type modes naturally appear in a finite-length nanorod structure [28,29]. By removing these short period fluctuations, we can identify three major absorption peaks as indicated by the black-solid curve at $\varepsilon=0$ for $\lambda < 700$ nm. These major absorption peaks correspond to LMRs [29], which are HE_{ml} for $m=1$ and $l=3, 4$, and 5 from right to left. Here, the subscripts m and l are the azimuthal and the radial mode number, respectively, in the circle. Note that HE_{ml} represents the TM-associated hybrid modes, which contribute dominantly to absorption when the incident wave vector is parallel to the wire-axis in the cylindrical nanowire. By exemplifying spatial distributions of two selected modes marked by the black arrows in Fig. 1(e), we can clearly confirm that these modes belong to the family of regular HE_{1l} modes at $\varepsilon = 0$, as shown in Figs. 1(f) and (g). On the other hand, at $\varepsilon=0.43$, we can identify a greater number of absorption peaks compared to that of $\varepsilon = 0$ (black-solid curve), as shown by the red-solid curve in Fig. 1(e). For the peaks marked by the red arrows in Fig. 1(e), the common structure of spatial distributions of chaotic modes is well demonstrated in Figs. 1(h) and (i). In the figure, we can see that they exhibit almost uncorrelated mode profiles with HE_{1l} modes, i.e., regular modes at $\varepsilon = 0$.

3.3. Light absorption enhancement

The light absorption efficiency depending on ε in nanowires is quantitatively estimated by defining a total absorption rate $\Gamma(R_0, \varepsilon)$ as

$$\Gamma(R_0, \varepsilon) \equiv \frac{1}{\mathcal{N}} \int_{\lambda_{\min}}^{\lambda_{\max}} \mathcal{A}(\varepsilon, \lambda) d\lambda = 1 - \mathcal{T} - \mathcal{R}, \quad (1)$$

where $\mathcal{N} (\equiv \lambda_{\max} - \lambda_{\min})$, \mathcal{T} , \mathcal{R} , and $\mathcal{A}(\varepsilon, \lambda)$ are the normalization factor, the transmittance, the reflectance, and the absorption rate at the parameters (ε, λ) , respectively. Now, we compute $\Gamma(R_0, \varepsilon)$ for the full deformation range, $0.0 < \varepsilon < 1.0$. A black-solid curve in Fig. 2(a) shows the total absorption rate (before the effect of FP-type modes is removed) as a function of ε , which gradually increases to the maximum value at $\varepsilon=0.43$. After this point, the ε -dependent value of $\Gamma(R_0 = 200$ nm, $\varepsilon)$ does not change significantly up to $\varepsilon=1.0$. That is, the total absorption

rate of a stadium-shaped cross-section is always higher than that of a circular one in nanowire arrays. In our computations, we obtain $\Gamma(R_0 = 200 \text{ nm}, \varepsilon = 0) = 0.45$ and $\Gamma(200 \text{ nm}, 0.43) = 0.55$, i.e. the total absorption rate at $\varepsilon = 0.43$ is 22% higher than that at $\varepsilon = 0.0$. To emphasize, obviously, this remarkable enhancement is induced just by the deformation of the wire cross-section; the deformation is the only parameter controlled in computations.

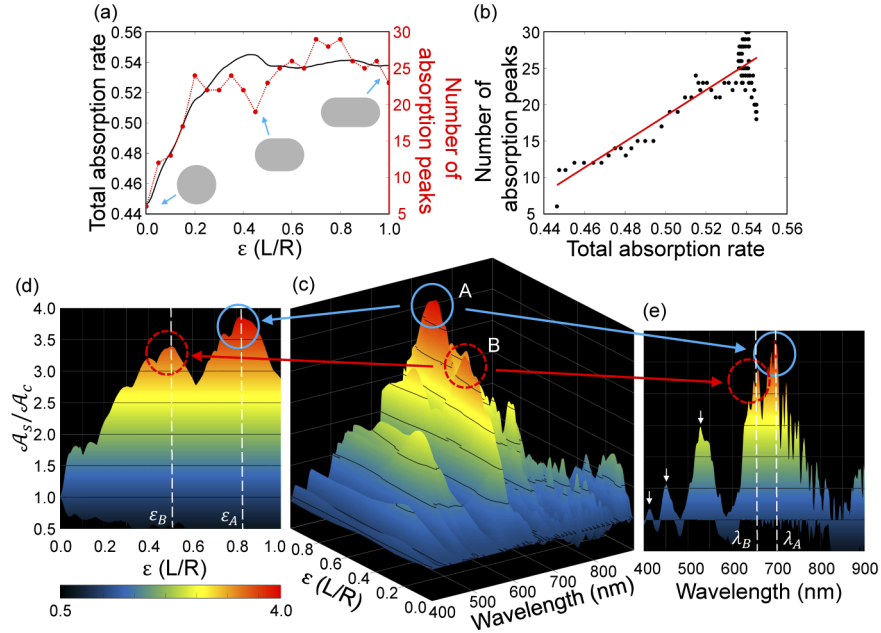


Fig. 2. The absorption rate and the number of absorption peaks depending on ε and λ . (a) The total absorption rate (black-solid curve) and the number of absorption peaks (red-dots) as a function of ε . (b) The correlation diagram between the total absorption rate and the number of absorption peaks. The overlaid red-solid curve is a least square linear fit to show linear dependency. (c) The fractional absorption rate $\mathcal{A}_s(\varepsilon, \lambda)/\mathcal{A}_c(\varepsilon = 0, \lambda)$, which is the absorption rate at (ε, λ) divided by the one at $(0, \lambda)$. (d) and (e) are the projection of (c) onto ε and λ planes, respectively. The blue-solid (A) and red-dashed circles (B) mark the first two maximum values of $\mathcal{A}_s/\mathcal{A}_c = 3.87$ and 3.39 at $(\varepsilon_A, \lambda_A) = (0.82, 696 \text{ nm})$ and $(\varepsilon_B, \lambda_B) = (0.51, 659 \text{ nm})$, respectively. (colorbar: $\mathcal{A}_s/\mathcal{A}_c$)

To examine the number of modes contributing to the total absorption rate, we count the total number of dominant peaks in the two polarization cases for 21 sampled values of ε after removing the peaks of FP modes. The details of this removing process is described in [Appendix](#). Through this process, we can suppress the small short-period peaks corresponding to the FP modes and obtain clean spectra containing only LMRs, as indicated by the solid curves in Fig. 1(e). The red-dots in Fig. 2(a) show the number of absorption peaks as a function of ε when the FP modes are filtered out. The correlation diagram between the number of peaks and the total absorption rate is given in Fig. 2(b). In this figure, one can see that they are under a strong positive correlation since the number of absorption peaks increases as ε increases monotonically. We found that the number of peaks and the total absorption rate are related by the Pearson correlation coefficient of 0.8628. We emphasize that the number of peaks cannot be translated directly to the total absorption rate because we did not take the different broadening and intensities of the peaks into account for the individual absorption mode. However, it is useful to see their definite proportionality qualitatively.

Although, the deformation-dependent total absorption rate obtained above already exhibits extraordinary enhancement, it turns out that the wavelength-resolved absorption efficiency can show even more surprising improvement at specific values of (ε, λ) . Figures 2(c), (d), and (e) reveal the fact that the wavelength-resolved absorption enhancement, which is given by the fractional absorption rate $[\equiv \mathcal{A}_s(\varepsilon, \lambda)/\mathcal{A}_c(\varepsilon = 0, \lambda)]$ reaches even up to almost "4"; 3.87 at $(\varepsilon_A, \lambda_A)=(0.82, 696 \text{ nm})$ and 3.39 at $(\varepsilon_B, \lambda_B)=(0.52, 659 \text{ nm})$. Moreover, as is shown in Fig. 2(e), this wavelength-resolved absorption enhancement manifests a high-contrast selectivity in absorption spectra, that is, such specific wavelengths, as marked by A, B, and arrows, can absorb much more light than other wavelengths. We believe this selectivity can be employed in versatile applications operated by wavelength-resolved signal detections.

4. Experimental results

4.1. Fabrication of free-standing nanowire arrays

For experiments of light absorption rate, our free-standing Si nanowire arrays are fabricated through the following process steps: Circle or stadium dot arrays are patterned by image reversal photolithography with an AZ5214 (AZ Electronic Materials) on n-Si wafers (Czochralski-grown, $525 \pm 25 \mu\text{m}$ thick, $\langle 111 \rangle$ orientation, Unisill Inc.). After deposition of Cr (150 nm) on the patterned Si, the residue is removed by acetone, resulting in Cr nanodot arrays as a metal mask for the Si nanowires. The Si is then etched by deep reactive ion etching (DRIE) (Tegal 200). The DRIE process is carried out using SF₆ (250 sccm)/C₄F₈ (150 sccm) in a cyclic etching mode and passivation with a 1500-W source power, using 40-mTorr gas pressure and 100-W stage power. The etching time is precisely controlled to get 10-, 20-, and 40- μm -thick Si nanowire. The Cr metal mask is removed with a Cr etchant after the DRIE process. Then, the nanowire arrays are coated with a solution containing 5.5 g hexamethylcyclotrisiloxane (Sigma Aldrich), 1 g PDMS (Sylgard 184, Dow Corning), 0.10 g PDMS curing agent, and 5 ml dichloromethane. The solution is spin-coated onto the samples at 600 rpm for 210 s and at 800 rpm for 10 s, and cured at 100 °C for 20 min. After curing, 40 wt% of KOH solution is injected to the bottom of the Si nanowire - PDMS to detach the composite film from the parent substrate. The KOH solution etched the $\langle 100 \rangle$ direction of $\langle 111 \rangle$ Si wafers, and thus the $\langle 111 \rangle$ wafer is laterally etched and the Si nanowire - PDMS composites are naturally detached from the Si parent substrate.

4.2. Optical characterization of circular and stadium-shaped of Si nanowire

The morphologies of the Si nanowire - PDMS composites were characterized by scanning electron microscopy (Quanta200FE-SEM, FEI). The experimental absorption rate was deduced by Eq. (1) as in the numerical computations: 100% - T (Transmittance) - R (Reflectance). All the optical characterizations were carried out by using a UV-vis-NIR spectrophotometer (Cary 5000, Agilent) with an internally Polytetrafluoroethylene coated integrating sphere to account for the total diffuse and specular light reflected or transmitted from the samples. Before measuring transmittance for the samples, the 100% transmission baseline was measured without sample, allowing the light to pass through the sphere. The average time for collecting the transmitted or reflected light at each interval is 0.3 s, and the data interval is 0.5 nm. The halogen lamp is used as a light source. For detecting the reflected and transmitted light, the R928 PMT detector is utilized according to the Cary 5000's default settings.

4.3. Free-standing Si-nanowire PDMS composites

For the experimental demonstration of the light absorption enhancement, we fabricate free-standing Si nanowire-PDMS composites for $\varepsilon=0$ and 0.24, as shown in the Scanning-Electron-Microscope (SEM) image and illustrations in Fig. 3. In order to suppress undesired effects of boundary defects, we set the parameters of the etching mask sufficiently large as $a = 4 \mu\text{m}$ and

$R_0 = 1.24 \mu\text{m}$ for three etching depths of $h = 10, 20$, and $40 \mu\text{m}$. Brief schematic views of the fabrication processes are orderly given in Fig. 3(a), (b) and (c).

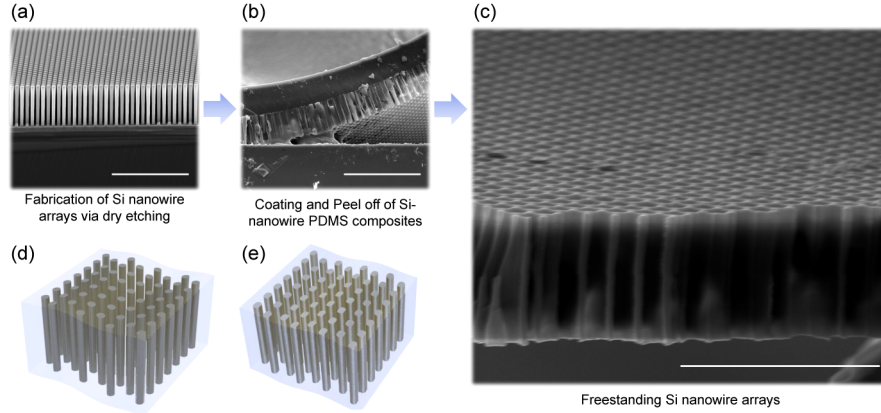


Fig. 3. (a) Patterned Si nanowire arrays via dry etching (scale bar: $50 \mu\text{m}$). (b) Detaching of the coated Si nanowire-PDMS composite from the wafer substrate (scale bar: $50 \mu\text{m}$). (c) Final structure of the transparent composite of free-standing Si nanowire arrays and PDMS (scale bar: $30 \mu\text{m}$). (d) and (e) Schematic view of the circular and the stadium-shaped Si nanowire-PDMS composite, respectively.

Figures 4(a) and (b) are SEM images of the patterned cylindrical and stadium-shaped nanowires in arrays for $\varepsilon=0$ and 0.24 , respectively. To clearly demonstrate the cross-section shapes of fabricated wires, here, we present SEM images of wires taken before PDMS is coated. For constructing our sample structures as regularly as possible with respect to the pitch of arrays, we take the hexagonal cell structure for the array. Figure 4(c) shows the experimentally measured absorption rate [$\mathcal{A}(\varepsilon, \lambda) \equiv 1 - \mathcal{T}(\varepsilon, \lambda) - \mathcal{R}(\varepsilon, \lambda)$] of the circular (dotted curve) and the stadium-shaped (solid curve) nanowires for three different heights. In the figure, one can see that the absorption rate of the stadium-shaped nanowire is always higher than that of the circular ones in the same height for all the cases of height. Because a longer wire contains a larger volume of silicon, the absorption rate of a longer wire is higher than that of a shorter one, as shown in the figure.

Our experimental results consistently prove the fact that the absorption rate of stadium-shaped nanowires is significantly higher than that of the circular ones: The total absorption rates of the circle, $\Gamma(R_0 = 1.24 \mu\text{m}, \varepsilon = 0)$ for $h = 10, 20$, and $40 \mu\text{m}$, are obtained as 0.4203 , 0.5967 , and 0.6858 , respectively, and those of the stadium $\Gamma(1.24 \mu\text{m}, 0.24)$ are 0.4910 , 0.6457 , and 0.7161 . Therefore, we can deduce that the enhancements of the light absorption rate, $\frac{\Gamma(R_0=1.24 \mu\text{m}, \varepsilon=0.24) - \Gamma(1.24 \mu\text{m}, 0)}{\Gamma(1.24 \mu\text{m}, 0)} \times 100\%$, are 16.83% , 8.22% , and 4.42% . These different values imply that the volume of silicon contained in wires grows as the wire height increases along z -direction. The experimental absorption rate is summarized in Table 1 in comparison to FDTD simulations. The wavelength-resolved absorption enhancement is given in Fig. 4(d) for three height cases. In the figure, we can see that the enhancement can be higher by above 20% in region, roughly, $600 \text{ nm} < \lambda$ for $h = 10 \mu\text{m}$. Particularly, at the longer wavelength of $\lambda \sim 800 \text{ nm}$, the enhancement reaches up to about 25% . The height-dependent decreasing trend already observed in Fig. 4(c) is also clearly visible in d. Here, we note the observation of regime change around $\lambda_c \sim 480 \text{ nm}$ (vertical dashed line), which separates the weak and strong enhancement regimes of $\lambda < \lambda_c$ and $\lambda > \lambda_c$, respectively. This critical wavelength of λ_c is a virtual border, where the dispersion of the refractive index and extinction coefficient of Si changes steeply. Below λ_c , the extinction coefficient of Si is much higher than the one in the region above λ_c , and because of this

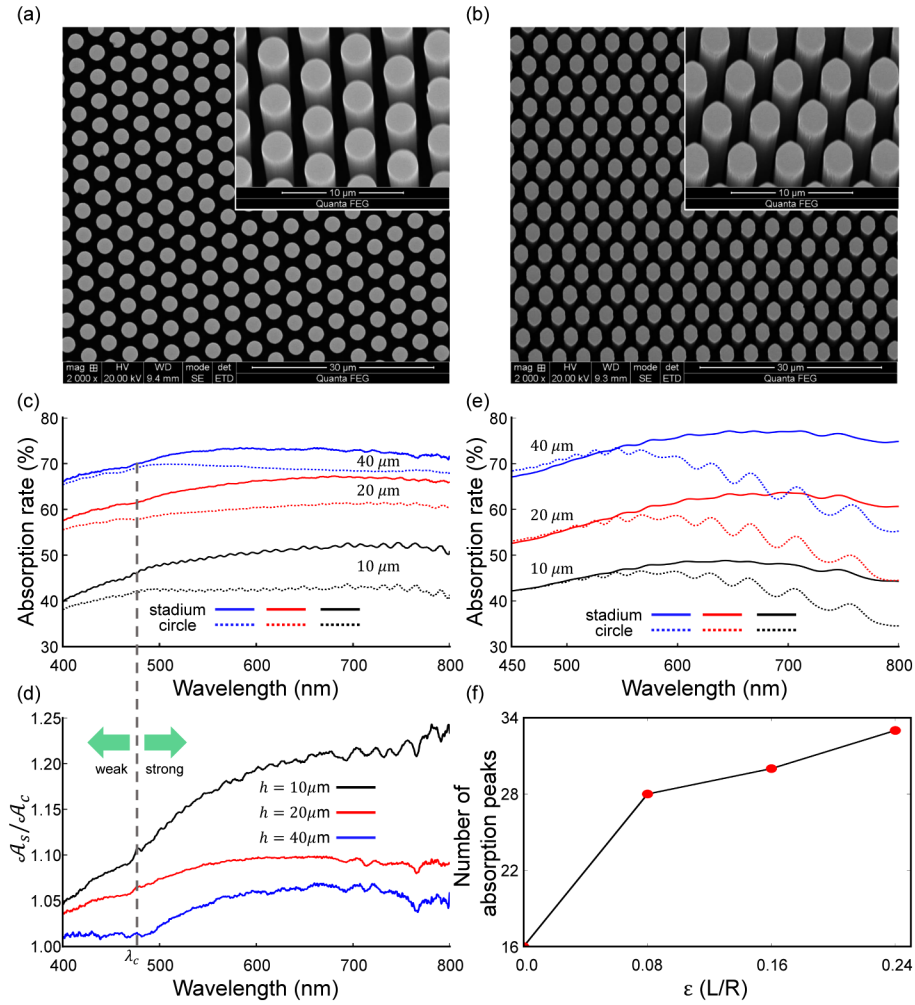


Fig. 4. The SEM images of the circular and the stadium-shaped nanowires in arrays and the experimental absorption rate depending on the wavelength for three cases of wire height $h = 10, 20$, and $40 \mu\text{m}$. (a) and (b) are SEM images of the circular and the stadium-shaped nanowires, respectively. (c) is the experimentally measured absorption rate of the nanowire arrays as a function of wavelength λ . The black, red, and blue dotted (solid) curves are for the circular (stadium) nanowires of heights 10, 20, and $40 \mu\text{m}$, respectively. (d) The experimentally measured fractional absorption rate $\mathcal{A}_s(\varepsilon = 0.24, \lambda)/\mathcal{A}_c(\varepsilon = 0, \lambda)$ as a function of λ for the three wire height cases. The dashed vertical line marks λ_c separating the strong and weak absorption enhancement regimes. (e) The numerically obtained absorption spectra for the same structural parameters used in the experiments. The spectra in (e) are polished by the averaging process (see text). (f) The number of absorption peaks as a function of the deformation parameter ε for the fixed height $h = 10 \mu\text{m}$.

material property, the light absorption process is quickly completed before the resonance effect is predominant in the light absorption mechanism. These experimental results are well supported and reproduced by our numerical simulations carried out by the same systems parameters used in the experiments, as shown by the spectra in Fig. 4(e). In obtaining these spectra, we first apply the Fourier filtering, as shown in Fig. 9, then the running-average of the original spectra is taken in order to make the comparison with the experimental results more visible. After these spectral

polishing techniques, the peaks with a small-amplitude and a short-period can be suppressed, while the one with a large-amplitude and a long-period can be moderated. The further numerical case-studies of the deformation-dependent number of absorption peaks are given in Fig. 4(f). In these studies, the constant height and the cross-sectional area that match the experimental parameters are used. As we can see in the figure, the number of absorption peaks grows as the deformation increases, and this result is consistent with the one for the case of the smaller area of the cross-section with $R_0 = 200$ nm in Fig. 2. Therefore, we can conclude that the number of absorption peaks, i.e., absorption channels, in nanowire arrays is augmented as the deformation increases regardless of the cross-sectional area, i.e, R_0 , and accordingly, the absorption rate is enhanced.

Table 1. Comparison of the total absorption rate of nanowire arrays between experiments and simulations in the circular and stadium-shaped cross-section cases when $R_0 = 1.24 \mu\text{m}$, $a = 4 \mu\text{m}$, and $\varepsilon = 0.24$.

Height	$h = 10 \mu\text{m}$		$h = 20 \mu\text{m}$		$h = 40 \mu\text{m}$	
Shape of cross-section	Exp.	Sim.	Exp.	Sim.	Exp.	Sim.
Circle	0.4203	0.4059	0.5967	0.5161	0.6858	0.6414
Stadium	0.4910	0.4553	0.6457	0.5988	0.7161	0.7411

5. Discussion

Thus far, we have elucidated the fact that a greater number of modes in chaotic wires contribute to the light absorption process, and hence, the absorption rate increases compared to circular wires. The significant enhancement is clearly verified in experiments, as well. However, because the process behind how the coupling mechanism functions for the enhancement in detail is not yet turned out explicitly, here, we will give detailed explanations for it. Basically, the core mechanism operates in terms of two different types of mode interaction, the Demkov [31] and the Landau-Zener type; they are clarified in Appendix exemplifying a nanowire array with the radius $R_0 = 100$ nm, height $h = 4 \mu\text{m}$, and pitch $a = 1 \mu\text{m}$. Now, we will remark on several interesting findings in resonance dynamics in Figs. 1(c) and (d). First, the modes in the dashed boxes bifurcate into two separate peaks moving in opposite directions, as ε increases. This bifurcation originates from the interaction referred to as Demkov-type coupling. Second, in the dashed ellipses, two modes repulse each other along a sharp avoided crossing. This type of short-range repulsion is the representative property of Landau-Zener-type coupling. Third, after the repulsion, one of the two curves eventually disappears. Finally, the modes in the dotted circles are newly emerging ones, which are absent at $\varepsilon=0$. The last two phenomena are also associated with the Landau-Zener-type coupling: only one mode can contribute to absorption before the interaction. Then, during an avoided crossing process, two interacting modes form symmetric and anti-symmetric superpositions of them exchanging their original mode properties. Hence, the other mode can contribute to the absorption rate only when this mode is in the superposed state with the original-contribute mode at around the avoided crossing point.

From the results obtained, it becomes clear that both Demkov-type and Landau-Zener-type mode interactions triggered by the chaotic cross-sectional shape of a nanowire induce an increasing number of absorption peaks. Such interactions are generic features of a chaotic system, and hence, we had carried out further case-studies for various other chaotic shapes of the cross-section – a quadrupole [32], a spiral [33], a limaçon [34], and a rounded D-shaped [35] – and confirmed a robust enhancement of absorption efficiency consistently. We are going to report these additional results elsewhere soon.

6. Conclusion

In summary, we have revealed that the light absorption efficiency of nanowires is dramatically enhanced when the cross-sectional morphology of the wires is chaotic. As the deformation strength of the chaotic cross-section increases, more and more absorption channels are opened, as LMRs exhibit bifurcations and avoided crossings. These characteristic resonance dynamics depending on a deformation parameter, result in enriched peak structures in an absorption spectrum of chaotic nanowires. These complicated spectral structures contribute to the enhancement of the total light absorption rate by up to 22.0% (calculation for $R_0 = 200\text{nm}$) and 16.8% (experiment for $R_0 = 1.24\mu\text{m}$). Through the experiments, a noticeable enhancement of the absorption rate in chaotic nanowires has been confirmed. It is emphasized that there is no restriction on the size or materials because our finding is solely concerned with the morphology (wave-chaos phenomenon) of the wire cross-section. We believe that the findings in the present paper will provide invaluable knowledge for optimizing various wire-structure-based devices requiring highly efficient light absorption.

Appendix

Fourier filtering of Fabry-Perot modes

In the absorption spectra, the small-amplitude short-period fluctuations imprinted on the large-amplitude long-period oscillations are identified. This small fluctuation originates from the FP modes while the large one the LMR modes. The removing process of the FP modes in the absorption spectrum is carried out in three steps. First, the spectrum is transformed from the wavelength λ domain to the wavenumber k domain, by the relation $k = 2\pi/\lambda$. Then the spectrum is Fourier transformed to the length domain. This transformed spectrum is referred to as the length spectrum [36]. Second, we truncate the spectrum up to the length shorter than the length of FP modes (twice the height of wire). Third, after applying the inverse Fourier transformation to the truncated length spectrum, we recover the original spectrum in the wavelength domain. As a result, the small fluctuations are removed.

An absorption spectrum in which short period Fabry-Perot type modes are not excluded is shown in Fig. 5(a). By excluding the Fabry-Perot type modes, we can see clear LMR peaks, as shown in Fig. 5(b). Now, we can count the number of LMRs in Fig. 5(b) for each linear polarization. In the figures, the blue-dotted and the red-dotted curves are the absorption spectra when the polarization of incident light is along the major and the minor axis, respectively. The black-solid spectrum is the average of the two dotted curves representing the case of unpolarized incident light.

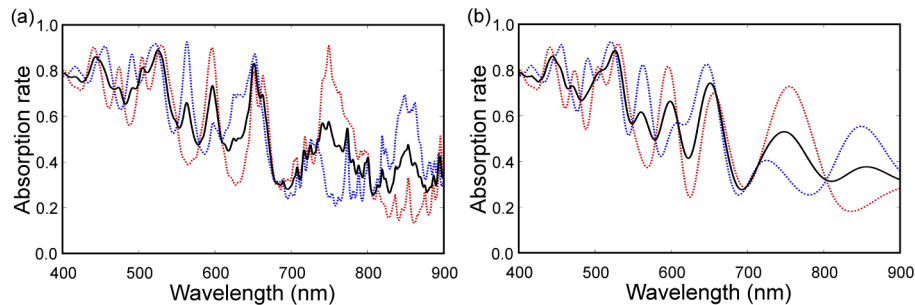


Fig. 5. (a) and (b) The absorption spectra for $R_0 = 200\text{nm}$ nanowire arrays at $\varepsilon = 0.43$ including and excluding Fabry-Perot type modes, respectively. The blue-dotted and the red-dotted spectrum are the absorption spectrum when the polarization of the incident light is along the major and the minor axis, respectively. The black-solid spectrum is the average of the two dotted curves representing the case of unpolarized incident light.

black-solid curve represents the average of the two polarization cases, i.e., unpolarized incident light.

Two types of avoided crossings: Demkov and Landau-Zener couplings

To elucidate a more explicit mechanism of the bifurcations and the emerging of new modes for augmented absorption channels, we exemplify the absorption spectrum of smaller radius (compared to $R_0 = 200$ nm simulated in the main text) nanowires by FDTD simulations. Note that the smaller radius nanowire allows a smaller number of LMRs in which we can investigate the resonance dynamics depending on deformation more clearly. For this purpose, we compute the absorption spectra of nanowire arrays having the radius $R_0 = 100$ nm, the height $h = 4$ μm , and the pitch $a = 1$ μm as a function of ε in the range $400 \leq \lambda \leq 700$ nm. Figure 6 is ε -dependent absorption spectra. In the figure, the two most prominent absorption peaks labeled by A and B are located around $\lambda = 401.96$ and 518.36 nm, respectively, at $\varepsilon = 0$. These two peaks correspond to $\text{HE}_{ml} = \text{HE}_{13}$ and HE_{12} , respectively.

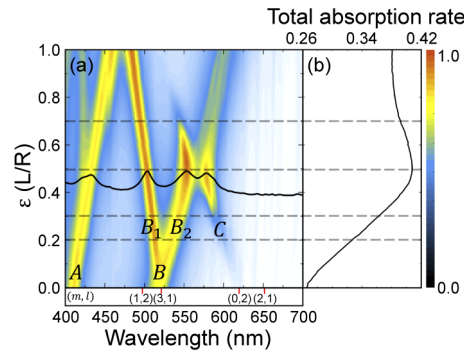


Fig. 6. The absorption spectra of nanowire arrays as a function of ε and λ , and The total absorption rate as a function of ε . (a) The curves labelled by A, B, C, B_1 , and B_2 are the absorption peaks exhibit bifurcations, an avoided crossing, emerging of a new mode, and disappearing of a mode due to coupling. (b) The total absorption rate of the nanowire array as a function of ε .

By tracing the absorption spectrum, a number of branching curves are identified, as the deformation increases from $\varepsilon = 0.0$ to 1.0 . At $\varepsilon = 0.3$, the four prominent absorption peaks labelled by A, B_1 , B_2 , and C are observed around 423.28, 509.92, 543.40, and 587.28 nm, respectively, as shown in Fig. 6(a). Here, the HE_{12} mode labeled by B bifurcates into the two separate peaks moving in an opposite direction, as ε increases (blue shift of peak B_1 and red shift of peak B_2). The HE_{13} mode labeled by A also bifurcates into the two separate peaks around $\varepsilon = 0.5$. The curve of peak C is a newly emerging one around $\varepsilon = 0.12$, which is absent at $\varepsilon = 0$. Around $\varepsilon = 0.48$, the curves B_2 and C repulse each other. This repulsion associates with avoided crossings (ACs). The curve B_2 eventually disappears around $\varepsilon = 0.8$. Due to these phenomena, the total absorption rate, $\Gamma(100 \text{ nm}, \varepsilon)$, increases monotonically (with a relatively steep slope) from 0.265 at $\varepsilon = 0$ to 0.408 at $\varepsilon = 0.48$, and then decreases monotonically (with a relatively gentle slope) after this maximum point as ε increases further, as shown in Fig. 6(b). In this nanowire array, the maximum enhancement of the total absorption rate reaches up to 54% at $\varepsilon = 0.48$.

The underlying mechanism of the phenomena mentioned above is attributable to the mode coupling process and is identical to the ones of phenomena observed in Figs. 1(c) and (d) in the main text. The bifurcation of curve B into B_1 and B_2 is caused by Demkov-type mode interaction. The repulsion between the curves B_2 and C along a sharp AC is caused by the Landau-Zener-type

mode interaction. The emerging of the curve C and disappearing of curve B_2 are due to the AC. The curve C emerges only around the AC point, and the curve B_2 disappears after the AC since the modes of the curves B_2 and C exchange their properties over the AC. Demkov and Landau-Zener type interactions can be proven by wavefunction analyses.

The ε -dependent dynamics of the absorption spectrum can be explained in terms of mode coupling mechanisms among LMRs. The mode coupling can be explained by using superpositions of spatial distributions of modes. The spatial distributions of modes B_1 and B_2 at $\varepsilon = 0.2$ for the fixed height $z_0 = 2.0 \mu\text{m}$ are shown in Figs. 7(a) and (b), respectively. As is shown in the figure, although these modes are bifurcated from the same point B at $\varepsilon = 0.0$, the morphologies of their spatial distributions are quite different. When we let the wavefunction of the mode B at $\varepsilon = 0.0$ for the fixed height $z_0 = 2.0 \mu\text{m}$ be $\psi_B(x, y)$ and that of the modes B_1 and B_2 at $\varepsilon = 0.2$ be $\psi_{B1}(x, y)$ and $\psi_{B2}(x, y)$, we can obtain superpositions of modes $(\psi_{B1} \pm \psi_{B2}) / \sqrt{2}$, as shown in Fig. 7(c) and (d), respectively. The morphologies of these artificial superpositions resemble those of modes HE_{12} and HE_{31} , as shown in Figs. 7(e) and (f), respectively. It should be noted that the HE_{31} mode cannot be excited when the incident light is parallel to the wire axis. However, HE_{31} can be excited for lateral incident light. This result implies that two nearly degenerated modes of HE_{12} and HE_{31} at $\varepsilon = 0.0$, i.e., at the mode B in Fig. 6(a) before the bifurcation, interact with each other generating the coupled modes ψ_{B1} and ψ_{B2} at $\varepsilon \neq 0.0$. The morphologies of the coupled mode pair maintain even when ε increases further. This type of interaction is referred to as Demkov-type coupling.

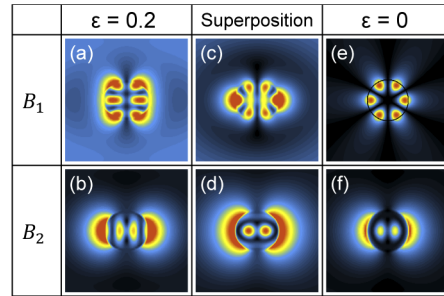


Fig. 7. The spatial distribution of electric field intensities of modes B_1 and B_2 on the cross-section at the fixed height $2 \mu\text{m}$ of the nanowire when the polarization of the incident light is parallel to the major axis. (a) and (b) The morphology of modes B_1 and B_2 at $\varepsilon = 0.2$, respectively, which are bifurcated from mode B . (c) and (d) The morphology of superposed modes $(\psi_{B1} \pm \psi_{B2}) / \sqrt{2}$, respectively. (e) and (f) The mode of (3,1) and (1,2) at $\varepsilon = 0.0$, respectively. The mode shown in (e) cannot be observed at $\varepsilon = 0$ when the incident light is parallel to the nanowire axis. This mode can be observed only when the incident light is lateral.

The interacting modes with a coupling v can be expressed in terms of uncoupled basis modes. If we assume that this coupling v is introduced to a well-isolated two-level system, Hamiltonian can read:

$$\mathcal{H} = \begin{pmatrix} e_0 - \delta & v \\ v^* & e_0 + \delta \end{pmatrix}, \quad (2)$$

whose eigenvalues are $e_{\pm} = e_0 \pm \sqrt{\delta^2 + |v|^2}$. $e_0 \pm \delta$ is the unperturbed energy of basis state parameterized by a detuning $\pm\delta$ from the median value e_0 when $v = 0$. Corresponding eigenstates $(c_1, c_2)^T$ of $|\Psi\rangle = c_1|\psi_1\rangle + c_2|\psi_2\rangle$ are

$$\begin{pmatrix} c_1^\pm \\ c_2^\pm \end{pmatrix} = \left[|v|^2 + \left(\mp\delta + \sqrt{\delta^2 + |v|^2} \right)^2 \right]^{-1/2} \times \begin{pmatrix} \mp\delta + \sqrt{\delta^2 + |v|^2} \\ \pm |v| \end{pmatrix}, \quad (3)$$

where $|\psi_i\rangle$ and c_i are the corresponding initial basis eigenstate and the amplitude of superposition when $v \neq 0$ satisfying $|c_1^\pm|^2 + |c_2^\pm|^2 = 1$, respectively. If the two states are nearly degenerate, i.e. $|\delta| \ll |v|$, the eigenstates of \mathcal{H} can be given as $(c_1, c_2)^T \approx 1/\sqrt{2}(1, \pm 1)^T$. This means that linear superpositions of the initial basis states with equal amplitude of c_1 and c_2 are the eigenstates of Hamiltonian under the sufficiently strong coupling strength v .

To investigate the coupling behavior around AC at $\varepsilon = 0.48$, we examine ψ_{B_2} at $\varepsilon = 0.3$, 0.48, and 0.7 shown in Figs. 8(a), (c), and (g) and examine ψ_C shown in Figs. 8(b), (d), and (h), respectively. At the AC point, $\varepsilon = 0.48$, the two coupled modes ψ_{B_2} and ψ_C exhibit the superpositions of the original modes, which can be obtained by the reverse superpositions of the modes ψ_{B_2} and ψ_C , i.e., $(\psi_{B_2} \pm \psi_C)/\sqrt{2}$, as shown in Figs. 8(e) and (f), respectively. These artificial superpositions resemble the morphologies of ψ_{B_2} and ψ_C at $\varepsilon = 0.7$ as well as those of ψ_C and ψ_{B_2} at $\varepsilon = 0.3$, respectively. Across this short-range AC process, the mode profiles of B_2 and C are exchanged with each other. This is the representative property of Landau-Zener-type coupling, which takes place along a sharp AC. The mode property of curve B_2 ($\varepsilon < 0.48$) is shared in a finite AC region, where the emergence of curve C is induced. Hence, after AC, the curve B_2 containing the mode property that was in B_2 before AC, disappears after this AC. In other words, B_2 and C exchange their mode property over the short-ranged AC.

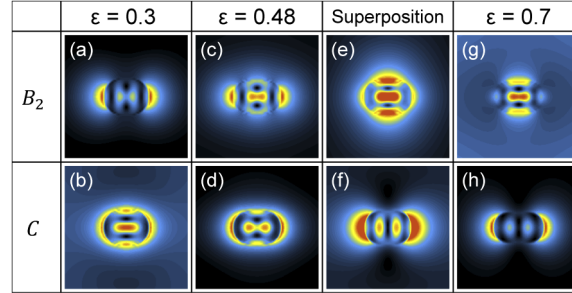


Fig. 8. The spatial distribution of electric field intensities of modes B_2 and C on the cross-section at the fixed height $2 \mu\text{m}$ of the nanowire when the polarization of the incident light is parallel to the major axis. (a) and (b) The morphology of modes B_2 and C at $\varepsilon = 0.3$, respectively. (c) and (d) The morphology of modes B_2 and C at $\varepsilon = 0.48$, respectively. (e) and (f) The morphology of superposed modes $(\psi_{B_2} \pm \psi_C)/\sqrt{2}$ at $\varepsilon = 0.48$, respectively. (g) and (h) The morphology of modes of B_2 and C at $\varepsilon = 0.7$, respectively. In this figure, although the deformation parameters are different, we can see that the properties of modes (a) and (b) are exchanged for the ones of the modes (g) and (h) after an AC. Also, the superposed modes (e) and (f) are similar to the modes (b) and (a) as well as the modes (g) and (h), respectively. This is the typical property of Landau-Zener-type mode interaction.

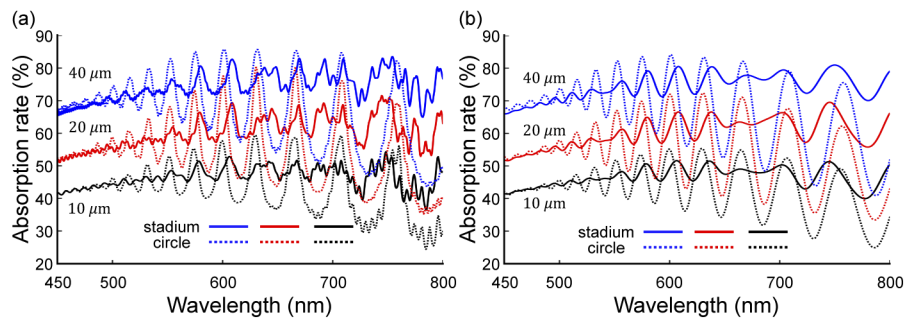


Fig. 9. (a) is the numerical absorption spectrum of the nanowire arrays for $R_0 = 1.24\mu\text{m}$. (b) is the Fourier filtered absorption spectrum from (a). The black, red, and blue dotted (solid) curves are the absorption spectra for the circular (stadium) nanowires of heights 10, 20, and $40\mu\text{m}$, respectively. The deformation parameter for the stadium cross-sectional nanowire is set to $\varepsilon = 0.24$.

Funding

National Research Foundation of Korea (2019M1A2A2072416, NRF-2018R1A2B2003720); Korea Institute of Energy Technology Evaluation and Planning (20163010012450, 20193091010460); Ministry of Health and Welfare (HG18C0069).

Acknowledgment

K. J. Choi, C. M. Kim, and C. H. Yi equally contributed to this work as a corresponding author.

Disclosures

The authors declare no conflicts of interest.

References

1. S. W. Eaton, A. Fu, A. B. Wong, C.-Z. Ning, and P. Yang, "Semiconductor nanowire lasers," *Nat. Rev. Mater.* **1**(6), 16028 (2016).
2. Y. Cui, Q. Wei, H. Park, and C. M. Lieber, "Nanowire nanosensors for highly sensitive and selective detection of biological and chemical species," *Science* **293**(5533), 1289–1292 (2001).
3. M. D. Kelzenberg, D. B. Turner-Evans, B. M. Kayes, M. A. Filler, M. C. Putnam, N. S. Lewis, and H. A. Atwater, "Photovoltaic measurements in single-nanowire silicon solar cells," *Nano Lett.* **8**(2), 710–714 (2008).
4. A. I. Kuznetsov, A. E. Miroschnichenko, M. L. Brongersma, Y. S. Kivshar, and B. Luk'yanchuk, "Optically resonant dielectric nanostructures," *Science* **354**(6314), aag2472 (2016).
5. H. Park, Y. Dan, K. Seo, Y. J. Yu, P. K. Duane, M. Wober, and K. B. Crozier, "Filter-free image sensor pixels comprising silicon nanowires with selective color absorption," *Nano Lett.* **14**(4), 1804–1809 (2014).
6. L. Cao, P. Fan, E. S. Barnard, A. M. Brown, and M. L. Brongersma, "Tuning the color of silicon nanostructures," *Nano Lett.* **10**(7), 2649–2654 (2010).
7. L. Cao, J.-S. Park, P. Fan, B. Clemens, and M. L. Brongersma, "Resonant germanium nanoantenna photodetectors," *Nano Lett.* **10**(4), 1229–1233 (2010).
8. B. C. Sturmberg, K. B. Dossou, L. C. Botten, A. A. Asatryan, C. G. Poulton, R. C. McPhedran, and C. M. De Sterke, "Optimizing photovoltaic charge generation of nanowire arrays: a simple semi-analytic approach," *ACS Photonics* **1**(8), 683–689 (2014).
9. Y. Yu, V. E. Ferry, A. P. Alivisatos, and L. Cao, "Dielectric core-shell optical antennas for strong solar absorption enhancement," *Nano Lett.* **12**(7), 3674–3681 (2012).
10. A. Mohammad, S. R. Das, M. R. Khan, M. A. Alam, and D. B. Janes, "Wavelength-dependent absorption in structurally tailored randomly branched vertical arrays of insb nanowires," *Nano Lett.* **12**(12), 6112–6118 (2012).
11. S.-K. Kim, R. W. Day, J. F. Cahoon, T. J. Kempa, K.-D. Song, H.-G. Park, and C. M. Lieber, "Tuning light absorption in core/shell silicon nanowire photovoltaic devices through morphological design," *Nano Lett.* **12**(9), 4971–4976 (2012).
12. S.-K. Kim, X. Zhang, D. J. Hill, K.-D. Song, J.-S. Park, H.-G. Park, and J. F. Cahoon, "Doubling absorption in nanowire solar cells with dielectric shell optical antennas," *Nano Lett.* **15**(1), 753–758 (2015).

13. M. D. Kelzenberg, S. W. Boettcher, J. A. Petykiewicz, D. B. Turner-Evans, M. C. Putnam, E. L. Warren, J. M. Spurgeon, R. M. Briggs, N. S. Lewis, and H. A. Atwater, "Enhanced absorption and carrier collection in si wire arrays for photovoltaic applications," *Nat. Mater.* **9**(3), 239–244 (2010).
14. H. Bao and X. Ruan, "Optical absorption enhancement in disordered vertical silicon nanowire arrays for photovoltaic applications," *Opt. Lett.* **35**(20), 3378–3380 (2010).
15. Z. Fan, R. Kapadia, P. W. Leu, X. Zhang, Y. L. Chueh, K. Y. K. Takei, A. Jamshidi, A. A. Rathore, D. J. Ruebusch, M. Wu, and A. Javey, "Ordered arrays of dual-diameter nanopillars for maximized optical absorption," *Nano Lett.* **10**(10), 3823–3827 (2010).
16. B. Wang and P. W. Leu, "Enhanced absorption in silicon nanocone arrays for photovoltaics," *Nanotechnology* **23**(19), 194003 (2012).
17. M. Ko, S.-H. Baek, B. Song, J.-W. Kang, S.-A. Kim, and C.-H. Cho, "Periodically diameter-modulated semiconductor nanowires for enhanced optical absorption," *Adv. Mater.* **28**(13), 2504–2510 (2016).
18. S. B. Kang, J.-H. Kim, M. H. Jeong, A. Sanger, C. U. Kim, C.-M. Kim, and K. J. Choi, "Stretchable and colorless freestanding microwire arrays for transparent solar cells with flexibility," *Light: Sci. Appl.* **8**(1), 121 (2019).
19. R. W. Day, M. N. Mankin, R. Gao, Y.-S. No, S.-K. Kim, D. C. Bell, H.-G. Park, and C. M. Lieber, "Plateau-rayleigh crystal growth of periodic shells on one-dimensional substrates," *Nat. Nanotechnol.* **10**(4), 345–352 (2015).
20. H.-C. Lee, J.-Y. Na, Y.-J. Moon, J.-S. Park, H.-S. Ee, H.-G. Park, and S.-K. Kim, "Three-dimensional grating nanowires for enhanced light trapping," *Opt. Lett.* **41**(7), 1578–1581 (2016).
21. J.-S. Park, K.-H. Kim, M.-S. Hwang, X. Zhang, J. M. Lee, J. Kim, K.-D. Song, Y.-S. No, K.-Y. Jeong, J. F. Cahoon, S.-K. Kim, and H.-G. Park, "Enhancement of light absorption in silicon nanowire photovoltaic devices with dielectric and metallic grating structures," *Nano Lett.* **17**(12), 7731–7736 (2017).
22. C. Liu, A. Di Falco, D. Molinari, Y. Khan, B. S. Ooi, T. F. Krauss, and A. Fratalocchi, "Enhanced energy storage in chaotic optical resonators," *Nat. Photonics* **7**(6), 473–478 (2013).
23. J. Huang, C. Liu, Y. Zhu, S. Masala, E. Alarousu, Y. Han, and A. Fratalocchi, "Harnessing structural darkness in the visible and infrared wavelengths for a new source of light," *Nat. Nanotechnol.* **11**(1), 60–66 (2016).
24. H.-J. Stöckmann, *Quantum chaos: an introduction* (Cambridge University Press, 2000).
25. G. Shaw, "Degeneracy in the particle-in-a-box problem," *J. Phys. A: Math., Nucl. Gen.* **7**(13), 1537–1546 (1974).
26. M. Tabor, *Chaos and Integrability in Nonlinear Dynamics: An Introduction* (Wiley-Interscience, 1989).
27. M. V. Berry, "Regularity and chaos in classical mechanics, illustrated by three deformations of a circular 'billiard'," *Eur. J. Phys.* **2**(2), 91–102 (1981).
28. K. T. Fountaine, W. S. Whitney, and H. A. Atwater, "Resonant absorption in semiconductor nanowires and nanowire arrays: Relating leaky waveguide modes to bloch photonic crystal modes," *J. Appl. Phys.* **116**(15), 153106 (2014).
29. B. Wang and P. W. Leu, "Tunable and selective resonant absorption in vertical nanowires," *Opt. Lett.* **37**(18), 3756–3758 (2012).
30. A. W. Snyder and J. Love, *Optical waveguide theory* (Springer, 1983), 1st ed.
31. F. Arranz, F. Borondo, and R. Benito, "Avoided crossings, scars, and transition to chaos," *J. Chem. Phys.* **107**(7), 2395–2406 (1997).
32. C.-H. Yi, J.-H. Kim, H.-H. Yu, J.-W. Lee, and C.-M. Kim, "Fermi resonance in dynamical tunneling in a chaotic billiard," *Phys. Rev. E* **92**(2), 022916 (2015).
33. S.-Y. Lee, S. Rim, J.-W. Ryu, T.-Y. Kwon, M. Choi, and C.-M. Kim, "Quasiscattered resonances in a spiral-shaped microcavity," *Phys. Rev. Lett.* **93**(16), 164102 (2004).
34. C.-H. Yi, M.-W. Kim, and C.-M. Kim, "Lasing characteristics of a limaçon-shaped microcavity laser," *Appl. Phys. Lett.* **95**(14), 141107 (2009).
35. J.-W. Lee, C.-H. Yi, M.-W. Kim, J. Ryu, K.-R. Oh, and C.-M. Kim, "Unidirectional emission of high-q scarred modes in a rounded d-shape microcavity," *Opt. Express* **26**(26), 34864–34871 (2018).
36. E. Bogomolny, N. Djellali, R. Dubertrand, I. Gozhyk, M. Lebental, C. Schmit, C. Ulysse, and J. Zyss, "Trace formula for dielectric cavities. ii. regular, pseudointegrable, and chaotic examples," *Phys. Rev. E* **83**(3), 036208 (2011).